Dalton Transactions

ROYAL SOCIETY OF CHEMISTRY

PAPER

View Article Online
View Journal | View Issue

Cite this: *Dalton Trans.*, 2024, **53**, 15491

Electrochemical approach of the reductive activation of O_2 by a nonheme Fe^{II} complex. Some clues for the development of catalytic oxidations†

Antoine Bohn,[a] Amanda Lyn Robinson,[a] Katell Sénéchal-David,[a] Christian Herrero,[a] Frédéric Kanoufi,[b] Elodie Anxolabéhère-Mallart[c] and Frédéric Banse *[a]

Received 28th June 2024,
Accepted 22nd August 2024

DOI: 10.1039/d4dt01870b

rsc.li/dalton

We report an in-depth study of the reductive activation of O_2 by the nonheme $[Fe^{II}(L^2_5)(MeCN)]^{2+}$ complex carried out by cyclic voltammetry. Experimental evidence is obtained for the slow coordination of dioxygen to the ferrous center yielding an Fe^{II}/O_2 adduct with a strong Fe^{II}–O_2 character rather than an Fe^{III}–superoxo one. Electron injection in the Fe^{II}–O_2 species occurs at a potential of *ca.* −700 mV *vs.* SCE, *i.e.* 200 mV above the O_2 to $O_2^{\bullet-}$ reduction, leading to the formation of a Fe^{III}–peroxo intermediate and then Fe^{III}–hydroperoxo upon protonation by residual water. The experimental CVs recorded at variable scan rate or variable Fe^{II} concentration are well simulated taking into account a detailed mechanism initiated by the competitive reduction of O_2 and the Fe^{II}–O_2 adduct. Analysis of the concentration of the reaction intermediates generated as a function of the applied potential indicates that the Fe^{III}–peroxo intermediate significantly accumulates at a potential of −650 mV. Oxidative bromination of anisole is assayed under electrolytic conditions at this potential to yield bromoanisole products. The low faradaic yields observed reveal that deleterious reactions such as direct reduction of reaction intermediates likely occur. Based on the detailed mechanism elucidated, a number of improvements to achieve more efficient catalytic reactions can be proposed.

Introduction

Oxidation reactions are used on a large scale for the synthesis of many commodities from abundant hydrocarbon feedstock.[1] However, these transformations are commonly performed with stoichiometric amounts of potent oxidizing reagents, thereby leading to the generation of huge amounts of side products.[2,3] Alternatively, dioxygen can be used as an oxidant but high temperature and pressure are required for its activation in order to bypass the spin forbidden reaction with singlet ($S = 0$) spin state organic molecules.[4] Due to the inherent conditions under which aerobic oxidations are carried out, they are energy consuming and frequently non selective at the same time. On the other hand, in Nature, many oxidative transformations are performed by metalloenzymes under physiological conditions. These natural systems are therefore an extraordinary source of inspiration for chemists interested in the development of sustainable oxidations. These enzymes activate dioxygen at a redox metal center in their active site (generally iron or copper) to generate potent oxidizing intermediates capable of oxygenating metabolites/xenobiotics with high efficiency and selectivity.[5–8] In the case of the nonheme iron enzymes Rieske dioxygenases, the metal center promotes the controlled reduction of O_2 *via* two sequential electron transfers from the terminal reductant NAD(P)H to generate the reactive oxidizing species. The catalytic cycle is initiated by the coordination of O_2 to the reduced Fe^{II} active site yielding a Fe^{III}–superoxo ($Fe^{III}(OO^{\bullet})$) intermediate which then undergoes an electron/proton transfer leading to an Fe^{III}–hydroperoxo ($Fe^{III}(OOH)$) complex. It is proposed that this latter intermediate directly performs the oxygen atom transfers to the substrate or after heterolytic O–O cleavage to yield an active Fe^{V}–oxo–hydroxo ($Fe^{V}(O)(OH)$).[9–12] Similar steps are encountered in the mechanism of many oxygenases with various active sites, *i.e.* dinuclear in methane monooxygenase[13] or heme in cytochromes P450.[14] In each case, O_2 activation relies on the controlled input of reducing equivalents at the active site to ensure the formation of the oxidizing reaction intermediates.

[a]*Université Paris-Saclay, CNRS, Institut de Chimie Moléculaire et des Matériaux d'Orsay, 91400 Orsay, France. E-mail: frederic.banse@universite-paris-saclay.fr*
[b]*Interfaces, Traitements, Organisation et Dynamique des Systèmes, Université de Paris, CNRS, F-75013 Paris, France*
[c]*Laboratoire d'Electrochimie Moléculaire, Université de Paris, CNRS, F-75013 Paris, France*

†Electronic supplementary information (ESI) available: Materials and methods, complete experimental procedures, CV simulations. See DOI: https://doi.org/10.1039/d4dt01870b

Eventually, the electron injection is only possible in the presence of the target substrate which serves as a fuse for the oxidizing species and allows preventing their direct reduction by the electron source and self-oxidation of the protein matrix at the same time.[15] Interestingly, nonheme α-ketoglutarate dependent halogenases catalyze the conversion of C–H into C–Cl or C–Br bonds following a similar dioxygen activation in the presence of halides (however, with some differences regarding the electron source and oxidation state of the active intermediate).[16,17]

Despite a comprehensive understanding of the mechanisms in Nature, it is difficult to reproduce this so-called reductive activation of O_2 with synthetic complexes that lack an elaborate supramolecular organisation allowing the orchestration of electron and proton consumption with the efficient oxidation of the substrate.[18,19] In contrast, to achieve the catalytic oxidation of small organic molecules by dioxygen, synthetic iron (II) complexes frequently promote autoxidation reactions instead of activating O_2 *via* inner sphere electron transfer.[20,21] The cases of catalytic O_2 activation by nonheme iron(II) complexes are rare and implement α-hydroxy acids[22,23] or the organic substrate[24] as sacrificial electron donors, mimicking alpha-ketoglutarate dependent enzymes[5] or tryptophan 2,3-dioxygenase,[25,26] respectively. Regarding the first category of catalysts, it was shown that the catalytic efficacy is limited due to the proton-induced catalyst deactivation or the competitive oxidation of α-hydroxy acids. For the second category, the catalytic systems are unselective, yielding a variety of products and the reactions proceed slowly and require thermal activation. Given the difficulty of controlling O_2 reactivity, reduced forms of oxygen, such as peroxides, are generally used in biomimetic studies with iron complexes.[3,8,27]

Electrochemical methods have been only scarcely used to deliver the electrons required for O_2 activation.[28] However, such methods potentially present several benefits: (i) a better control of the reaction steps, thanks to the analytical information that can be gathered from the electrical current; and (ii) a minimization of the reaction by-products, thanks to the use of O_2 as oxidant and the absence of a chemical reducing agent. Implementing a combination of electrochemical and spectroscopic techniques, we have demonstrated that nonheme[29] or heme[30] iron(III)–peroxo intermediates can indeed be generated at the electrode surface following this approach. More recently, we have reported on the epoxidation or chlorination of cyclooctene upon O_2 electrochemical reductive activation by a Mn porphyrin complex.[31]

Fe^{II} complexes with neutral tetradentate (N_4) or pentadentate (N_5) amine/pyridine ligands are frequently used for the activation of chemical oxidants in order to perform catalytic oxidations, mechanistic investigations or the characterization of their reaction-intermediates.[3,32,33] These complexes are generally air-stable but can activate O_2 in the presence of a convenient hydrogen donor or electron donor/acid combination.[34–38] In the particular case of Fe/L_5^2 systems (L_5^2 = *N*,*N*,*N*′-tris(2-pyridylmethyl)-*N*′-methyl-ethane-1,2-diamine) in the presence of air and ascorbate, single-strand cleavage on plasmid DNA was observed.[39] Therefore, such complexes appear as relevant precursors for the development of catalytic oxidations by dioxygen under electrolytic conditions. Additionally, using the $Fe^{II}(L_5^2)$ precursor, (hydro)peroxo and oxo–iron species can be generated in high yield and isolated to serve as reference species for the mechanistic study of oxygen activation.

In this paper, we report a thorough mechanistic investigation of the reaction of O_2 with the $Fe^{II}(L_5^2)$ complex by cyclic voltammetry (CV). Capitalizing on this study, attempts were made to brominate anisole. While our results indicate that this type of complex cannot efficiently activate O_2 under electrolytic conditions, they provide valuable indications for the development of more efficient catalysts following this strategy.

Results and discussion

Previous work in our lab demonstrated that the reaction of $[Fe^{II}(L_5^2)(MeCN)]^{2+}$ (**1**) (Scheme 1) with H_2O_2 leads to the accumulation of $[Fe^{III}(OOH)(L_5^2)]^{2+}$ which displays a reversible acid/base equilibrium with $[Fe^{III}(OO)(L_5^2)]^{+}$.[40–42] We have also previously reported that the reaction of **1** with single O-atom donors (PhIO, *m*CPBA) quantitatively yielded $[Fe^{IV}(O)(L_5^2)]^{2+}$.[43] Being able to generate, accumulate and, in some cases purify these reaction intermediates, allowed us to study their electrochemical and spectroscopic properties (see ESI, Fig. S3 and S4†). Therefore, the established reactivity of **1** and the electrochemical and spectroscopic data for the reactive species mentioned above can be used as benchmarks for the reaction between **1** and O_2 under reductive conditions.

Behaviour of complex 1 in presence of dioxygen: nature of the Fe^{II}–O_2 adduct

In MeCN at 20 °C, $[Fe^{II}(L_5^2)(MeCN)]^{2+}$ (**1**) displays a reversible Fe^{III}/Fe^{II} wave at $E_{1/2}$ = 0.94 V *vs.* SCE and a quasi-reversible Fe^{II}/Fe^{I} wave at −1.64 V (Fig. S1†). The Fe^{III}/Fe^{II} redox potential largely exceeds the arbitrary threshold value for the direct reac-

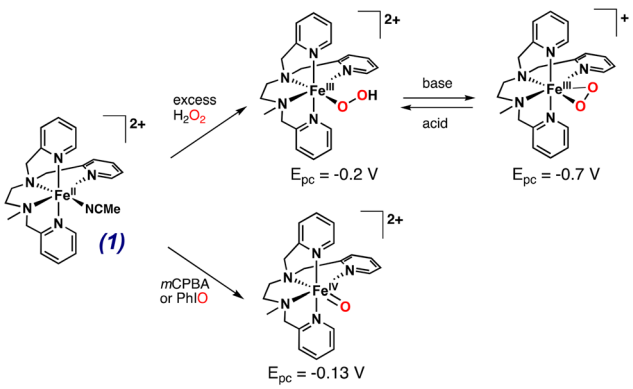

Scheme 1 Reactivity of complex **1**, $[Fe^{II}(L_5^2)(MeCN)]^{2+}$ with different chemical oxidants to form iron–oxygen species. Redox potentials are given *vs.* SCE.

tion of a non-heme Fe^{II} complex with O_2 which was estimated to be *ca.* 0.3 V *vs.* SCE.[44] In line with this value, the Fe^{II} complex **1** is air stable. Indeed, bubbling O_2 in an acetonitrile solution over 24 hours at room temperature does not lead to any modification (intensity or shape) of the $t_{2g}(Fe^{II})$-to-π*(pyridines) charge transfer band (data not shown). However, some complexes displaying potentials significantly larger than 0.3 V actually react with O_2,[45,46] as it was recently argued that the Fe^{III}/Fe^{II} redox potential value is not the only criterion to consider, but that the rate constant for the reaction of an Fe^{II} center with O_2 must also be taken into account.[19] Complex **1** displays a significant lability due to a LS (S = 0) to HS (S = 2) equilibrium with a 70%/30% distribution in solution at room temperature, as determined by magnetic moment measurement *via* the Evans method (Fig. S2†). Thus, **1** is susceptible to bind with O_2 following a reversible reaction to yield a Fe^{II}/O_2 adduct. As reported earlier, the description of Fe^{II}/O_2 species requires to consider multiple configurations.[47,48] For simplification, we only consider the two extreme ones corresponding to ferrous–dioxygen (Fe^{II}–O_2, Pauling description)[49,50] and ferric–superoxo ($Fe^{III}(OO^{\bullet})$, Weiss description).[51] Here, an $Fe^{III}(OO^{\bullet})$ species does not accumulate upon reaction between **1** and O_2, as evidenced by the lack of new spectroscopic feature which is expected in that case.[52–56] Therefore, we tentatively propose that the Fe^{II}/O_2 adduct displays a strong Fe^{II}–O_2 character rather than an $Fe^{III}(OO^{\bullet})$ one. This proposition is in line with the high Fe^{III}/Fe^{II} redox potential: the Fe^{II} center is not reducing enough to transfer an electron to the bound O_2 molecule, and the forward reaction in the **1** + O_2 ⇄ Fe^{II}–O_2 equilibrium is likely to be slow as no spectroscopic changes are evidenced. Unlike UV-vis spectroscopy, cyclic voltammetry operates under a dynamic regime, thus providing information on the formation of a Fe^{II}–O_2 species. Under argon, the normalized intensity of the anodic peak of the Fe^{III}/Fe^{II} wave for **1** recorded at various scan rates is constant indicating that the concentration of **1** probed at the electrode is not dependent on the scan rate (Fig. 1C). By contrast, this evolution recorded in the presence of O_2 is not linear, in line with the presence of an additional Fe^{II} species in equilibrium with **1** + O_2, *i.e.* an Fe^{II}–O_2 adduct (Fig. 1 and ESI, Scheme S1† for rationalization of the CVs using a square scheme mechanism). Even if the coordination of O_2 appears unfavored, electron injection in the Fe^{II}–O_2 species is expected to drive the reaction towards intermediates susceptible to participate in the oxidative transformations of substrates.

Reduction of dioxygen in the presence of 1: mechanistic analysis

To test this assumption, the CV of O_2 (1.6 mM in MeCN)[57] was recorded in the presence of increasing amounts of **1**, up to one equiv. *vs.* O_2 (Fig. 2). As soon as **1** is introduced in the solution, the $O_2/O_2^{\bullet-}$ redox wave ($E_{1/2}$ = −0.89 V, red trace) is modified with the development of a cathodic signal at E_{pc} = −0.75 V, the intensity of which depends on the concentration in **1**. At the same time, the progressive loss of $O_2/O_2^{\bullet-}$ reversibility is observed. Similar observations were made with a related complex, $[Fe^{II}(TPEN)]^{2+}$ (TPEN = *N*,*N*,*N*′,*N*′-tetrakis(2-pyridylmethyl)ethane-1,2-diamine), where the current intensity at −0.75 V was modelled and assigned to the reduction of the Fe^{II}–O_2 adduct.[29] Thus, the mechanism which was previously proposed to model the CVs of oxygenated solutions of $[Fe^{II}(TPEN)]^{2+}$ can serve as basis to the case of complex **1**. This

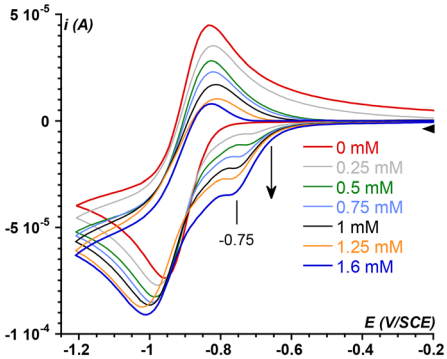

Fig. 2 CV of O_2 at a concentration of 1.6 mM (red) and in the presence of increasing equivalents of **1** in dry aerated CH_3CN at room temperature at a scan rate of 0.1 V s^{-1}. The concentration in **1** is indicated in the figure. The samples were initially scanned towards negative potentials.

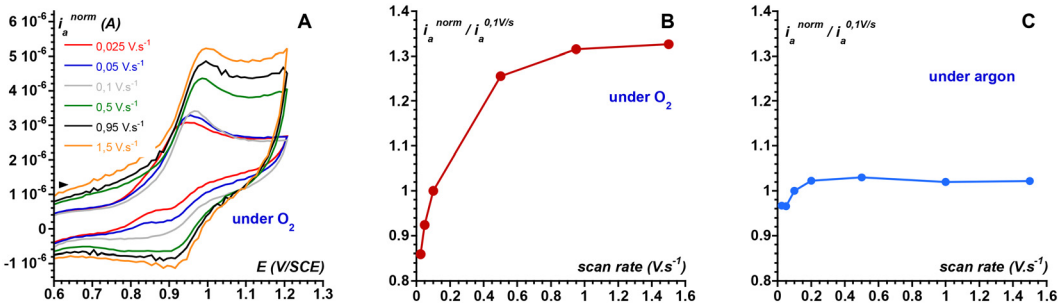

Fig. 1 (A) CV of the Fe^{III}/Fe^{II} signature of **1** (0.2 mM in O_2 saturated MeCN with 0.1 M $TBAPF_6$) at 20 °C at various scan rates. The CVs are normalized with respect to the one recorded at 0.1 V s^{-1}. (B) Ratio of the normalized anodic intensity of **1** under O_2 by its normalized anodic intensity at 0.1 V s^{-1} as a function of the scan rate. (C) Ratio of the normalized anodic intensity of **1** under argon by its normalized anodic intensity at 0.1 V s^{-1} as a function of the scan rate.

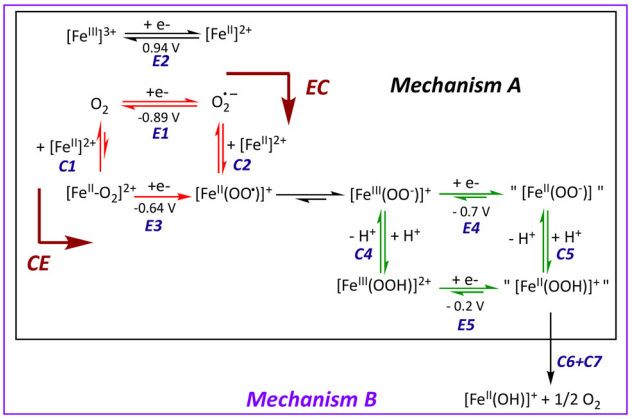

Scheme 2 Description of Mechanism A, black frame, and Mechanism B, purple frame, to model the experimental CVs for the reaction between O_2 and complex **1** (indicated as $[Fe^{II}]^{2+}$). The L_5^2 ligand has been omitted for clarity, but the global charge of each species is indicated. Except for the $[Fe^{II}–O_2]^{2+}$ adduct, the standard potential values indicated were determined independently by simulation of experimental CVs. All potential values are referred to SCE.

mechanism is shown in Scheme 2. It involves two square schemes, where electrochemical reactions (E) are represented as horizontal processes and chemical reactions (C) as vertical ones (Mechanism A in the black frame). The red square leads to a formal Fe^{II}–superoxide intermediate $Fe^{II}(OO^{\bullet})$ *via* either the reduction of the Fe^{II}–O_2 adduct (CE pathway), or the coordination of $O_2^{\bullet-}$, formed upon reduction of molecular oxygen at the electrode, to the Fe^{II} complex (EC pathway). The CE pathway reflects the development of the cathodic wave at −0.75 V, whereas the loss of reversibility of the $O_2/O_2^{\bullet-}$ wave in the presence of **1** supports the EC pathway. Additionally, since the $Fe^{II}(OO^{\bullet})$ species is not detected on the reverse scan (the cathodic wave at −0.75 V is not associated with an anodic signature), it is assumed that this species quickly evolves into its valence tautomer Fe^{III}–peroxo moiety ($Fe^{III}(OO^{-})$). This latter $Fe^{III}(OO^{-})$ species is the starting point of the second square scheme. In the green square scheme, the $Fe^{III}(OO^{-})$ intermediate undergoes either a CE pathway *via* $Fe^{III}(OOH)$ or EC pathway to a putative Fe^{II}–hydroperoxo species, where protons are supplied by the residual water present in the medium.‡

This mechanism was validated by simulating the experimental CVs. To limit the number of variable parameters, the CVs of the stable species (**1**, O_2) and independently generated intermediates ($[Fe^{III}(L_5^2)(OOH)]^{2+}$, $[Fe^{III}(L_5^2)(OO)]^{+}$ and $[Fe^{IV}(L_5^2)(O)]^{2+}$) were simulated separately beforehand to determine some of the standard potentials ($E°$) and electron transfer rates (k^0) (see ESI, Fig. S3 and S4† for the characterization of reaction intermediates and Fig. S15–S17† for experimental CVs and their simulation). As shown in Fig. 3, a satisfying simulation is obtained considering Mechanism A with the parameters listed in ESI, Fig. S5.† However, two key features observed in the experimental CVs are not well reproduced in the simulated ones. The reduction peak of O_2 into $O_2^{\bullet-}$ at *ca.* −1 V is not as intense in the simulation as it is in the experimental CV and the current intensity at the starting potential in the backward scan (−1.2 V) is likewise less intense in the simulation (see red arrows in Fig. 3). These observations indicate that the concentration of O_2 considered in Mechanism A is not large enough. Since $[O_2]$ is fixed to 1.6 mM in the simulation, corresponding to its solubility in MeCN,[57] the discrepancies between the simulated CV and the experimental data indicate that some O_2 is regenerated during the process, contributing to the current intensity. Therefore, additional reactions must be included to complement the mechanism.

We have recently reported that the one electron reduction of $[Fe^{III}(L_5^2)(OOH)]^{2+}$ results in the disproportionation of the hydroperoxo ligand to release O_2 (eqn (1)).[58,59]

$$2[Fe^{III}(OOH)(L_5^2)]^{2+} + 2e^- \rightarrow 2[Fe^{II}(OH)(L_5^2)]^{+} + O_2 \quad (1)$$

The $[Fe^{III}(L_5^2)(OOH)]^{2+}$ species is characterized by a cathodic peak at −0.2 V (ESI, Fig. S3†). As the reactions described in Mechanism A are triggered when the electrode is polarized at a potential below −0.7 V, *i.e.* lower than −0.2 V, the $[Fe^{III}(L_5^2)(OOH)]^{2+}$ must be readily reduced once formed, releasing dioxygen. Therefore, Mechanism A was modified to account for the disproportionation of $[Fe^{II}(L_5^2)(OOH)]^{+}$, yielding Mechanism B (Scheme 2 and Fig. 3 and ESI Fig. S6†). As expected, the Mechanism B results in a simulated CV that has a more intense cathodic peak at *ca.* −1 V for the reduction of O_2, and the reoxidation of $O_2^{\bullet-}$ on the backward scan is likewise more negative. However, a discrepancy between the simulated CV with the experimental one still persists, indicating

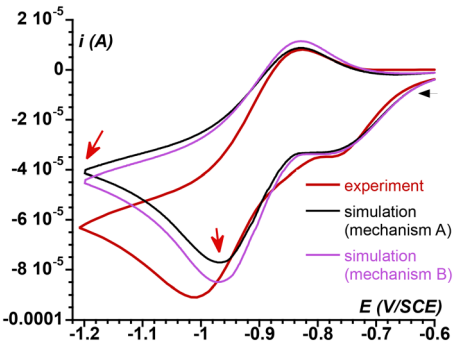

Fig. 3 CV of O_2 at a concentration of 1.6 mM in the presence of 1 equivalent of **1** in dry aerated CH_3CN at room temperature and a scan rate of 0.1 V s^{-1} (red line). Simulation with Mechanism A (black line) or Mechanism B (purple line). The initial direction of the scan is indicated by the black arrow. The red arrows highlight the discrepancies between experimental and simulated CVs, as discussed in the text.

‡Despite the use of dry acetonitrile, the concentration of water has been estimated to be 2 mM (see ESI,† "CV simulations" section). For electrolysis experiments its concentration has been increased. This is the only source of protons used in this study, as the optimization of proton-related parameters, *i.e.* acid strength and its delivery in the reaction mixture (one-shot or by using a syringe pump), nature of the conjugate base (coordinating or non-coordinating), corresponds to a complete study in itself.

that the disproportionation of $[Fe^{II}(L_5^2)(OOH)]^+$ does not account for all of the dioxygen probed at the electrode.

Considering all of the redox couples, written as horizontal reactions in Scheme 2, and their potential values (E° values indicated in Fig. S6, ESI†), it is clear that $O_2^{\bullet-}$ is the most reducing species. A simplified diagram indicating the E° values for the different redox couples is shown in Scheme 3. It highlights that reaction of $O_2^{\bullet-}$ with oxidizing species such as $[Fe^{III}(L_5^2)(OO)]^+$ or $[Fe^{III}(L_5^2)(OOH)]^{2+}$ will regenerate O_2 at the vicinity of the electrode. At the same time, Fe^{II} species such as $[Fe^{II}(L_5^2)(OO)]$ or $[Fe^{II}(L_5^2)(OOH)]^+$ will be released. The latter intermediate being susceptible to disproportionate into $[Fe^{II}(L_5^2)(OH)]^+$ and O_2 (eqn (1)), thereby leading to an increase of the cathodic current intensity at *ca.* −1 V. Moreover, in acetonitrile, the initial complex $[Fe^{II}(L_5^2)(MeCN)]^{2+}$ (**1**) can be easily regenerated from $[Fe^{II}(L_5^2)(OH)]^+$ to close the catalytic loop and initiate another series of reactions.

Fig. 4 presents the CVs response characterizing the oxidation of the species either present (black trace) in the oxygenated solution of **1**, or (red trace) produced near the electrode during a first cathodic cycle down to −1.2 V (*i.e.* as in Fig. 2). The CV of the pristine oxygenated solution of **1** (black trace) shows the signature of the reversible oxidation of $[Fe^{II}(L_5^2)(MeCN)]^{2+}$ (**1**) into $[Fe^{III}(L_5^2)(MeCN)]^{3+}$. When the same solution is first cycled towards the reduction peak of O_2, the oxidative signature of $[Fe^{II}(L_5^2)(MeCN)]^{2+}$ (**1**) significantly decreases in intensity by a factor of *ca.* 2. Additionally, a broad oxidation wave between 0.6 and 0.8 V appears, which is consistent with the presence in solution of $[Fe^{II}(L_5^2)(OH)]^+$ ($E_{p,a}$ = 0.66 V) and $[Fe^{II}(L_5^2)(OH_2)]^{2+}$ ($E_{p,a}$ = 0.84 V) as inferred from the electrochemical response of the reaction products of **1** with H_2O and a base (ESI, Fig. S7†). Because the total intensity for these two CVs (black and red traces, Fig. 4) is identical, this supports that $[Fe^{II}(L_5^2)(OH)]^+$ and $[Fe^{II}(L_5^2)(OH_2)]^{2+}$ are issued from the disproportionation reaction discussed above and that the regeneration of $[Fe^{II}(L_5^2)(MeCN)]^{2+}$ (**1**) from these species is slow on the CV timescale.

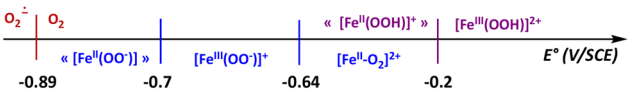

Scheme 3 Scale of negative redox potential values for the species involved in Mechanism B. All potential values are referred to SCE.

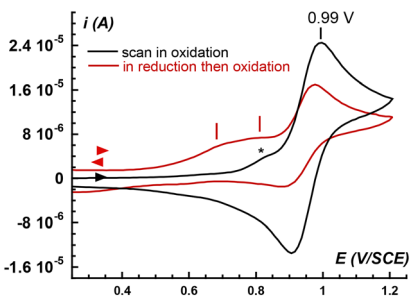

Fig. 4 CV of **1** at a concentration of 1.6 mM in O_2 saturated dry CH_3CN (at room temperature and a scan rate of 0.1 V s^{-1}). The sample has been scanned first toward anodic potentials (black line) or first toward cathodic potential, below the reduction of O_2 (–1.2 V) before scanning back toward anodic potentials (red line). The asterisk indicates a small amount of $[Fe^{II}(L_5^2)(OH_2)]^{2+}$ due to the presence of residual water.

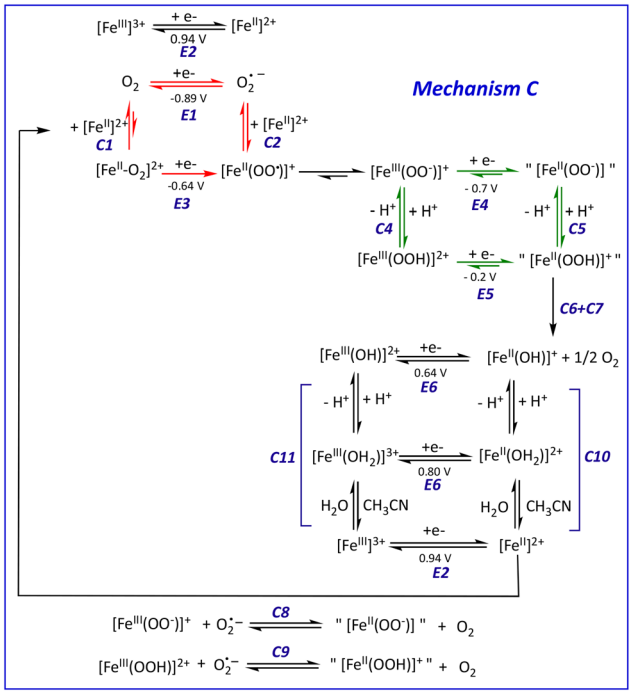

Scheme 4 Proposed Mechanism C, to model the experimental CVs for the reaction between O_2 and complex **1** (indicated as $[Fe^{II}]^{2+}$). The L_5^2 ligand has been omitted for clarity, but the global charge of each species is indicated. Except for the $[Fe^{II}–O_2]^{2+}$ adduct, the potential values indicated were determined independently by simulation of experimental CVs. All potential values are referred to SCE.

Thus, the series of redox reactions that implicate superoxide and Fe^{III} complexes (C8 and C9 in Scheme 4) as well as the chemical equilibria involving the Fe^{II} complexes evoked above (C10) and their Fe^{III} counterparts (C11) were considered.§ The new mechanism (Mechanism C) was used to further simulate the electrochemical response of the system under investigation. The parameters implemented in the simulations are tabulated in ESI Fig. S8† resulting in simulated CV that very satisfactorily matches the experimental CV on the negative potential range as well as the current intensity of the backward scan (Fig. 5A and B). To further check the validity of Mechanism C, CVs of solutions containing different O_2/**1** stoichiometric ratios were recorded and compared to their simulations based on Mechanism C. As displayed in Fig. 5C and D

§The equilibria between the $Fe^{III/II}(NCCH_3)$, $Fe^{III/II}(OH_2)$ and $Fe^{III/II}(OH)$ have been restricted to $Fe^{III/II}(NCCH_3)$ and $Fe^{III/II}(OH)$ for the sake of simplification (C10 and C11 in Scheme 4 and Fig. S8†). For the same reason, redox reactions have been restricted to two Fe^{III}/Fe^{II} couples (E2 and E6 in Scheme 4 and Fig. S8†).

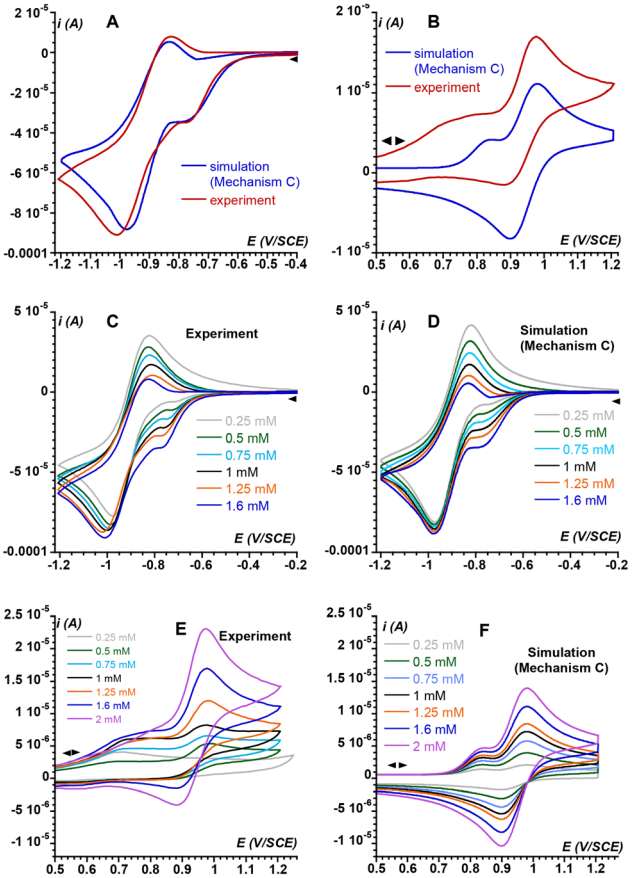

Fig. 5 CV of an equimolar mixture of **1** (1.6 mM) and O_2 in dry CH_3CN at room temperature and a scan rate of 0.1 V s^{-1} in the negative (A) and in the positive (B) potentials region. Experimental CVs (C) and their simulations (D) of **1** at various concentrations in the presence of O_2 (1.6 mM) in dry aerated CH_3CN at room temperature and a scan rate of 0.1 V s^{-1} in the negative potentials region. Experimental CVs (E) and their simulations (F) of **1** at various concentrations in the presence of O_2 (1.6 mM) in dry aerated CH_3CN at room temperature and a scan rate of 0.1 V s^{-1} in the positive potentials region. All the samples have been initially scanned toward negative potentials down to −1.2 V.

for the negative-potential region, and Fig. 5E and F for the positive region, the agreement is very good.

Interestingly, CVs recorded at various scan rates are also nicely simulated using Mechanism C (ESI, Fig. S9†). Thus, the most prominent electrochemical and chemical phenomena related to O_2 activation by **1** are encompassed in Mechanism C, which rules out the involvement of high valent $Fe^{IV}(O)$ species.¶ Therefore, such a species has not been considered to avoid over-parametrization of the system.

The further advantage of the CV simulation is that it allows better insights into the composition of the solution near the

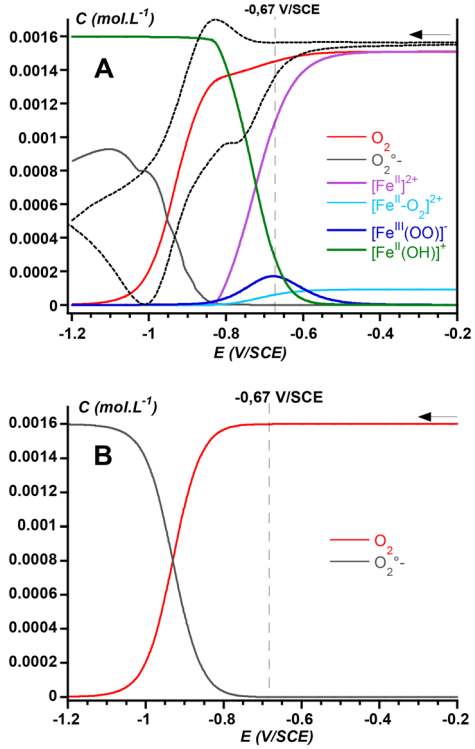

Fig. 6 (A) Simulated evolution of the concentration of the main species generated at the electrode surface when scanning an equimolar mixture of **1** and O_2 (1.6 mM, CH_3CN, RT, 0.1 V s^{-1}) between −0.2 and −1.2 V. The experimental CV is shown as the dashed black line on the same potential range (arbitrary intensity). (B) Evolution of the concentration of O_2 and $O_2^{\bullet-}$ when scanning a 1.6 mM acetonitrile solution of O_2 (RT, 0.1 V s^{-1}) between −0.2 and −1.2 V.

electrode surface, which provides important information for the development of electro-assisted oxidation reactions. Fig. 6 shows the evolution of the concentration of the predominant species generated at the electrode when a solution of **1** and O_2 is scanned from −0.2 V to −1.2 V *vs.* SCE. It depicts that consumption of O_2 (red trace) starts from *ca.* −0.6 V together with that of the Fe^{II} precursor **1** (purple trace). At the same time, the concentration in peroxo species $Fe^{III}(OO^-)$ increases and reaches its maximum at a potential of −0.67 V (dark blue). Interestingly, at this potential the direct production of superoxide from O_2 is negligible (see Fig. 6B), therefore showing that the $Fe^{III}(OO^-)$ intermediate is obtained *via* the CE pathway (Scheme 2), *i.e. via* steps catalyzed by the metal complex. For more negative potentials, the concentration of the $Fe^{III}(OO^-)$ peroxo species decreases while $[Fe^{II}(OH)]^+$ accumulates (green trace), reflecting the disproportionation of the $[Fe^{II}(OOH)]$ species formed by the reduction of the $Fe^{III}(OOH)$ complex. This latter intermediate is obtained by protonation of the $Fe^{III}(OO^-)$ species by residual water. While the generation of the $Fe^{III}(OOH)$ is supported by the overall Mechanism C, its concentration remains very low because water is a weak acid, and because it is readily reduced at such low potential values.

¶Disproportionation of $[Fe^{II}(L^2_5)(OOH)]^+$ at −50 °C has been shown to proceed through heterolytic cleavage of the O–O bond yielding an unstable $Fe^{IV}(O)$ intermediate before release of $[Fe^{II}(L^2_5)(OH)]^+$ and O_2 (see ref. 58). This highly reactive $Fe^{IV}(O)$ species is unlikely to accumulate significantly at 20 °C to contribute to the current intensity.

Table 1 Summary of the conditions used for the preparative scale electrolysis at −650 mV during 2 hours. The number of electrons accumulated per iron complex, the amount of brominated anisole product that was obtained, and the faradaic yield are indicated

Entry	Composition[a] **1** : anisole : Br^- : H_2O	[e^-] (mM)	e^-/Fe^{II}	[Product][b] (mM)	Faradic yield[c]
1	1 : 100 : 100 : 250	3.1	3.1	4-Br-anisole, 0.10 mM	6.5%
2	1 : 100 : 100 : 0	2.3	2.3	4-Br-anisole, 0.04 mM	3.5%
3	0 : 100 : 100 : 250	1.1	—	—	—
4	0 : 100 : 100 : 0	0.5	—	2-Br-anisole, 0.26 mM	104%

[a] 1 mM in **1** when present, TBABr used as Br^- source. [b] A mixture of the 3-bromoanisole is obtained, only the concentration of the main product is indicated. [c] Faradic yield = (2 × [product]/[e^-]) × 100.

Finally, Mechanism C indicates that O_2 activation by complex **1** involves two successive single electron transfers to generate Fe^{III}–peroxo species, which is reminiscent of Rieske dioxygenases[12,60] and P450.[14] In P450 enzymes, the Fe^{III}(OOH) Cpd0 evolves *via* O–O heterolysis towards CpdI, a formal Fe^{V}(O), which oxygenates the substrate while it is not yet clear whether the O-atom transfer activity is performed by the Fe^{III}(OOH) species in Rieske dioxygenases or whether it requires cleavage of the O–O bond. In our study, we found no evidence of O–O bond cleavage.

Attempted application in electrolysis for anisole bromination

This speciation of species is determined under CV conditions under diffusion regime, without stirring of the solution. It can be inferred that stirring may alter these concentration profiles and may help in transporting these species in the bulk solution where steady-state concentration could be reached.

Despite the fact that $Fe^{II}(L^2_5)$ and related complexes are efficient catalysts for the oxygenation of small organic substrates by H_2O_2,[61–65] our initial attempts to perform the electro-assisted oxygenation of small organic substrates such as ethylbenzene or cyclooctene in the presence of **1** were unsuccessful. At best, only trace amounts of products were obtained under these conditions. On an other hand, Vardhaman *et al.* reported that non-heme Fe^{III}(OOH) (obtained by reaction of a Fe^{II} precursor and excess H_2O_2) supported by pentadentate ligands were efficient oxidants for halides (I^-, Br^-, Cl^-) and could ultimately lead to the halogenation of aromatic molecules such as phenol red or anisole.[66,67] In line with these observations, we performed the spectrophotometric monitoring of the reaction of phenol red with Br^- in the presence of **1** and H_2O_2 to demonstrate that it indeed led to bromophenol blue (ESI, Fig. S10†). While the CVs simulation provided herein shows that the Fe^{III}(OOH) intermediate does not accumulate significantly, it can be generated *in situ* by protonation of its Fe^{III}(OO^-) conjugate base. Thus, we decided to assess our system in an aromatic bromination reaction. For this purpose, we used pure O_2 instead of air in order to increase the concentration of O_2 (8 mM)[57] and favor the formation of the Fe^{II}–O_2 and subsequent species, as well as a large excess of water as proton source and a carbon foam working electrode to significantly increase the electrode surface area (see ESI,† Materials and methods for complete experimental details). Based on the CV analysis, we performed the preparative scale electrolysis at −650 mV where the Fe^{III}(OO^-) intermediate is at its maximum concentration. Because phenol red is redox active at −600 mV *vs.* SCE, anisole was chosen as an alternative terminal aromatic hydrocarbon substrate.

Determination of the charge accumulated during the electrolysis of different reaction mixtures over 2 hours is depicted in ESI, Fig. S11.† In general, the presence of complex **1**, as well as the presence of water, led to a larger exchange of electrons. When both the complex and water were present, an equivalent of 3.1 mM electrons were exchanged in 2 hours, whereas it was slightly lower in the absence of water (Table 1, compare entries 1 and 2). Of note, the amount of Br-anisole formed is much lower than the amount of electrons supplied by the electrode, translating into a low faradaic yield. These observations indicate that most of the electrons are used for unproductive side reactions, such as reduction of reaction intermediates. Control experiments show that some products can be obtained in the absence of complex, but the faradaic yield exceeds 100% (entry 4), suggesting that some radical reactions are also likely to interfere in the process.‖ These radical processes are probably initiated by the generation of small amounts of superoxide at the electrode surface.

Lessons learned from the mechanistic analysis, the catalysis results, and possible improvements

A major drawback of the present system is that the activation of O_2 (reactions E3 and C3 in Scheme 4) corresponds to a simultaneous 2-electron transfer to dioxygen yielding the Fe^{III}(OO^-) intermediate. This activation is triggered at a low potential, close to or below the reduction of Fe^{III}(OO^-) or Fe^{III}(OOH) intermediates, respectively (reactions E4 and E5), resulting in the instability of these species. By contrast, in oxygenase enzymes, the two electron transfers are made sequentially which ensures the step-by-step progress of the catalytic cycle. To overcome this major drawback of the current system and achieve more efficient catalysis, the potentials at which the two electron transfers take place need to be tuned to each other.

First, using a more donating (*i.e.* anionic) ancillary ligand may stabilize Fe^{III} over Fe^{II}, hence significantly decreasing the

‖ Along the same line, we noticed that the H_2O_2-dependent bromination of phenol red catalyzed by **1** is more efficient under air than under argon.

Fe^{III}/Fe^{II} redox potential (E2 in Scheme 4) and promoting the coordination of O_2 to Fe^{II} by favoring an Fe^{II} to O_2 electron transfer. Thus, the first electron injection in O_2 would be triggered at a potential shifted toward more positive values, *i.e.* at the potential where Fe^{II} is generated, farther from the $O_2/O_2^{\bullet-}$ wave, resulting in a gain in energy and avoiding the generation of superoxide anions at the same time. In these conditions, the Fe^{II}/O_2 adduct would exhibit a predominant $Fe^{III}(OO^{\bullet})$ character instead of a Fe^{II}–O_2 one as in the present system. It is also conceivable that the use of an anionic ligand could lower the redox potential of the $Fe^{III}(OO^{-})$ and $Fe^{III}(OOH)$ intermediates (reactions E4 and E5) to allow their generation following electron transfer to the $Fe^{III}(OO^{\bullet})$ species while preventing their reduction, as observed in the current system. Along this line, starting from the heme $Fe^{III}(F_{20}TPP)Cl/O_2$ system, it has recently been shown that the injection of two electrons ultimately yielded a $Fe^{IV}(O)$ intermediate after O–O cleavage in a proposed $Fe^{III}(OOH)$ intermediate.[68]

A second possibility for tuning the redox potentials of the two electron transfers to O_2 would be to combine two different iron complexes so that each successively transfers one electron to dioxygen. We have evidenced this approach to be relevant for the aerobic sulfoxidation of thioanisole at a potential as high as −340 mV *vs.* SCE. In this reported study, we used a tandem system made of an Fe^{III} complex bearing an aminophenolato dianionic ligand designed to ensure the injection of the first electron to O_2, and of a Fe^{II} complex with a polyazadentate ligand to ensure the second electron transfer leading to a Fe^{III}–peroxo moiety.[69]

In addition to the electronic effects related to the first coordination sphere of the metal centre, the presence of functional groups aimed at developing hydrogen bonds in the second coordination sphere can provide further energy gain. For example, the presence of an OH group on the L_5^2 ligand resulted in a significant positive shift of the cathodic peak of the Fe^{II}–O_2 adduct, allowing to carry out the electroassisted oxidation of thioanisole at −500 mV *vs.* SCE.[70]

Finally, as the precise adjustment of the potentials associated with the 2 electron transfers may be difficult to achieve, pulsed electrolysis offers a complementary approach, where the application of short voltage steps at different potentials may allow the generation of reactions intermediates at applied potential E_1 and their preservation at applied potential E_2 to favour their reaction with the substrate. This methodology has recently been implemented in electrochemical CO_2 reduction.[71]

Conclusions

The detailed mechanism of reductive O_2 activation by $[Fe^{II}(L_5^2)(MeCN)]^{2+}$ (**1**) has been determined using a complete analysis and simulation of CVs. For consistency, this analysis was preliminary benchmarked by studying the electrochemical properties of the reaction intermediates that can be generated and stabilized from the Fe^{II} precursor. The generation of $Fe^{III}(OO^{-})$ and $Fe^{III}(OOH)$ intermediates is evidenced but this latter species does not accumulate significantly since O_2 activation is triggered at a potential where its reduction is favoured.

This system was assessed in preparative scale electrolysis for the bromination of anisole at a potential where the $Fe^{III}(OO^{-})$ intermediate is at its maximum concentration. While halogenation products are obtained, the faradaic yield is low indicating the occurrence of many unproductive side reactions. Taking advantage of the detailed mechanism, ways of improvement can be envisioned. Efforts in that sense are currently under investigation in our laboratory.

Data availability

The data used for this article are available on request from the authors.

Conflicts of interest

There are no conflicts to declare.

Acknowledgements

This work was supported by the Agence Nationale de la Recherche (GOAL Project, ANR-22-CE07-0037-01).

Notes and references

1 J. H. Teles, W. Partenheimer, R. Jira, F. Cavani, G. Strukul, R. Hage, J. W. Boer, L. Gooßen, P. Mamone and O. A. Kholdeeva, Oxidation, in *Applied Homogeneous Catalysis with Organometallic Compounds: A Comprehensive Handbook in Four Volumes, Third Edition*, Wiley, 1st edn, 2017, vol. 64.
2 T. A. Nijhuis, M. Makkee, J. A. Moulijn and B. M. Weckhuysen, *Ind. Eng. Chem. Res.*, 2006, **45**, 3447–3459.
3 G. Olivo, O. Cussó, M. Borrell and M. Costas, *J. Biol. Inorg. Chem.*, 2017, **22**, 425–452.
4 F. Cavani and J. H. Teles, *ChemSusChem*, 2009, **2**, 508–534.
5 S. Kal and L. Que, *J. Biol. Inorg. Chem.*, 2017, **250**, 625–627.
6 E. I. Solomon, D. E. Heppner, E. M. Johnston, J. W. Ginsbach, J. Cirera, M. Qayyum, M. T. Kieber-Emmons, C. H. Kjaergaard, R. G. Hadt and L. Tian, *Chem. Rev.*, 2014, **114**, 3659–3853.
7 A. J. Jasniewski and L. Que, *Chem. Rev.*, 2018, **118**, 2554–2592.
8 X. Huang and J. T. Groves, *Chem. Rev.*, 2018, **118**, 2491–2553.
9 Y. Wang, J. Li and A. Liu, *J. Biol. Inorg. Chem.*, 2017, **22**, 395–405.
10 P. C. A. Bruijnincx, G. van Koten and R. J. M. Klein Gebbink, *Chem. Soc. Rev.*, 2008, **37**, 2716.
11 B. S. Rivard, M. S. Rogers, D. J. Marell, M. B. Neibergall, S. Chakrabarty, C. J. Cramer and J. D. Lipscomb, *Biochemistry*, 2015, **54**, 4652–4664.

12 M. E. Runda, N. A. W. de Kok and S. Schmidt, *ChemBioChem*, 2023, **24**, e202300078.
13 V. C. C. Wang, S. Maji, P. P. Y. Chen, H. K. Lee, S. S. F. Yu and S. I. Chan, *Chem. Rev.*, 2017, **117**, 8574–8621.
14 B. Meunier, S. P. de Visser and S. Shaik, *Chem. Rev.*, 2004, **104**, 3947–3980.
15 T. L. Poulos, *Chem. Rev.*, 2014, **114**, 3919–3962.
16 F. H. Vaillancourt, E. Yeh, D. A. Vosburg, S. Garneau-Tsodikova and C. T. Walsh, *Chem. Rev.*, 2006, **106**, 3364–3378.
17 A. Timmins and S. P. de Visser, *Catalysts*, 2018, **8**, 314–325.
18 S. Sahu and D. P. Goldberg, *J. Am. Chem. Soc.*, 2016, **138**, 11410–11428.
19 D. C. Lacy, *Inorg. Chem. Front.*, 2019, **6**, 2396–2403.
20 P. Comba, Y.-M. Lee, W. Nam and A. Waleska, *Chem. Commun.*, 2014, **50**, 412.
21 M. Sankaralingam, Y.-M. Lee, W. Nam and S. Fukuzumi, *Inorg. Chem.*, 2017, **56**, 5096–5104.
22 S. Chatterjee, S. Bhattacharya and T. K. Paine, *Inorg. Chem.*, 2018, **57**, 10160–10169.
23 B. N. Sánchez-Eguía, J. Serrano-Plana, A. Company and M. Costas, *Chem. Commun.*, 2020, **56**, 14369–14372.
24 G. Liao, F. Mei, Z. Chen and G. Yin, *Dalton Trans.*, 2022, **51**, 18024–18032.
25 J. Geng, A. C. Weitz, K. Dornevil, M. P. Hendrich and A. Liu, *Biochemistry*, 2020, **59**, 2813–2822.
26 J. Basran, E. S. Booth, M. Lee, S. Handa and E. L. Raven, *Biochemistry*, 2016, **55**, 6743–6750.
27 J. Chen, W. Song, Y.-M. Lee, W. Nam and B. Wang, *Coord. Chem. Rev.*, 2023, **477**, 214945.
28 E. Anxolabéhère-Mallart and F. Banse, *Curr. Opin. Electrochem.*, 2019, **15**, 118–124.
29 N. Ségaud, E. Anxolabéhère-Mallart, K. Sénéchal-David, L. Acosta-Rueda, M. Robert and F. Banse, *Chem. Sci.*, 2014, **6**, 639–647.
30 R. Oliveira, W. Zouari, C. Herrero, F. Banse, B. Schöllhorn, C. Fave and E. Anxolabéhère-Mallart, *Inorg. Chem.*, 2016, **55**, 12204–12210.
31 N. Kostopoulos, F. Banse, C. Fave and E. Anxolabéhère-Mallart, *Chem. Commun.*, 2021, **57**, 1198–1201.
32 S. M. Hözl, P. J. Altmann, J. W. Kück and F. E. Kühn, *Coord. Chem. Rev.*, 2017, **352**, 517–536.
33 M. Guo, T. Corona, K. Ray and W. Nam, *ACS Cent. Sci.*, 2018, **5**, 13–28.
34 F. Li, K. M. V. Heuvelen, K. K. Meier, E. Münck and L. Que, *J. Am. Chem. Soc.*, 2013, **135**, 10198–10201.
35 A. Thibon, J. England, M. Martinho, V. G. Young, J. R. Frisch, R. Guillot, J.-J. Girerd, E. Münck, L. Que and F. Banse, *Angew. Chem., Int. Ed.*, 2008, **47**, 7064–7067.
36 M. Martinho, G. Blain and F. Banse, *Dalton Trans.*, 2010, **39**, 1630.
37 Y.-M. Lee, S. Hong, Y. Morimoto, W. Shin, S. Fukuzumi and W. Nam, *J. Am. Chem. Soc.*, 2010, **132**, 10668–10670.
38 S. Hong, Y.-M. Lee, W. Shin, S. Fukuzumi and W. Nam, *J. Am. Chem. Soc.*, 2009, **131**, 13910–13911.
39 P. Mialane, A. Nivorojkine, G. Pratviel, L. Azéma, M. Slany, F. Godde, A. Simaan, F. Banse, T. Kargar-Grisel, G. Bouchoux, J. Sainton, O. Horner, J. Guilhem, L. Tchertanova, B. Meunier and J.-J. Girerd, *Inorg. Chem.*, 1999, **38**, 1085–1092.
40 A. J. Simaan, F. Banse, P. Mialane, A. Boussac, S. Un, T. Kargar-Grisel, G. Bouchoux and J. J. Girerd, *Eur. J. Inorg. Chem.*, 1999, 993–996.
41 A. J. Simaan, S. Döpner, F. Banse, S. Bourcier, G. Bouchoux, A. Boussac, P. Hildebrandt and J.-J. Girerd, *Eur. J. Inorg. Chem.*, 2000, 1627–1633.
42 A. J. Simaan, F. Banse, J.-J. Girerd, K. Wieghardt and E. Bill, *Inorg. Chem.*, 2001, **40**, 6538–6540.
43 A. Bohn, C. Chinaux-Chaix, K. Cheaib, R. Guillot, C. Herrero, K. Sénéchal-David, J.-N. Rebilly and F. Banse, *Dalton Trans.*, 2019, **48**, 17045–17051.
44 S. Hong, Y.-M. Lee, K. Ray and W. Nam, *Coord. Chem. Rev.*, 2017, **334**, 25–42.
45 Y.-M. Chiou and L. Que, *J. Am. Chem. Soc.*, 1995, **117**, 3999–4013.
46 M. P. Mehn, K. Fujisawa, E. L. Hegg and L. Que, *J. Am. Chem. Soc.*, 2003, **125**, 7828–7842.
47 K. P. Jensen and U. Ryde, *J. Biol. Chem.*, 2004, **279**, 14561–14569.
48 K. P. Jensen, B. O. Roos and U. Ryde, *J. Inorg. Biochem.*, 2005, **99**, 45–54.
49 L. Pauling and C. D. Coryell, *Proc. Natl. Acad. Sci. U. S. A.*, 1936, **22**, 210–216.
50 L. Pauling, *Nature*, 1964, **203**, 182–183.
51 J. J. Weiss, *Nature*, 1964, **202**, 83–84.
52 X. Shan and L. Que, *Proc. Natl. Acad. Sci. U. S. A.*, 2005, **102**, 5340–5345.
53 F. Oddon, Y. Chiba, J. Nakazawa, T. Ohta, T. Ogura and S. Hikichi, *Angew. Chem.*, 2015, **127**, 7444–7447.
54 C.-W. Chiang, S. T. Kleespies, H. D. Stout, K. K. Meier, P.-Y. Li, E. L. Bominaar, L. Que, E. Münck and W.-Z. Lee, *J. Am. Chem. Soc.*, 2014, **136**, 10846–10849.
55 C. Winslow, H. B. Lee, M. J. Field, S. J. Teat and J. Rittle, *J. Am. Chem. Soc.*, 2021, **143**, 13686–13693.
56 A. A. Fischer, S. V. Lindeman and A. T. Fiedler, *Chem. Commun.*, 2018, **54**, 11344–11347.
57 J. M. Achord and C. Hussey, *Anal. Chem.*, 1980, **52**, 601–602.
58 A. Bohn, K. Sénéchal-David, J. Rebilly, C. Herrero, W. Leibl, E. Anxolabéhère-Mallart and F. Banse, *Chem. – Eur. J.*, 2022, **28**, e202201600.
59 H. P. H. Wong, F. Banse and S. P. de Visser, *ChemCatChem*, 2023, **15**, e202300957.
60 S. M. Barry and G. L. Challis, *ACS Catal.*, 2013, **3**, 2362–2370.
61 V. Balland, D. Mathieu, N. Pons-Y-Moll, J.-F. Bartoli, F. Banse, P. Battioni, J.-J. Girerd and D. Mansuy, *J. Mol. Catal. A: Chem.*, 2004, **215**, 81–87.
62 N. Ségaud, J.-N. Rebilly, K. Sénéchal-David, R. Guillot, L. Billon, J.-P. Baltaze, J. Farjon, O. Reinaud and F. Banse, *Inorg. Chem.*, 2013, **52**, 691–700.
63 A. Thibon, J.-F. Bartoli, S. Bourcier and F. Banse, *Dalton Trans.*, 2009, 9587.

64 A. Thibon, J.-F. Bartoli, R. Guillot, J. Sainton, M. Martinho, D. Mansuy and F. Banse, *J. Mol. Catal. A: Chem.*, 2008, **287**, 115–120.
65 R. Bercy, J. Rebilly, C. Herrero, R. Guillot, H. Maisonneuve and F. Banse, *Eur. J. Inorg. Chem.*, 2023, **26**, e202300236.
66 A. K. Vardhaman, C. V. Sastri, D. Kumar and S. P. de Visser, *Chem. Commun.*, 2011, **47**, 11044.
67 A. K. Vardhaman, P. Barman, S. Kumar, C. V. Sastri, D. Kumar and S. P. de Visser, *Chem. Commun.*, 2013, **49**, 10926–10923.
68 N. Kostopoulos, C. Achaibou, J.-M. Noël, F. Kanoufi, M. Robert, C. Fave and E. Anxolabéhère-Mallart, *Inorg. Chem.*, 2020, **59**, 11577–11583.
69 A. L. Robinson, J.-N. Rebilly, R. Guillot, C. Herrero, H. Maisonneuve and F. Banse, *Chem. – Eur. J.*, 2022, e202200217.
70 A. L. Robinson, E. Bannermann, R. Guillot, C. Herrerro, K. Sénéchal-David, E. Rivière, F. Banse and J.-N. Rebilly, *Eur. J. Inorg. Chem.*, 2024, **27**, e202300694.
71 F. Greenwell, B. Siritanaratkul, P. K. Sharma, E. H. Yu and A. J. Cowan, *J. Am. Chem. Soc.*, 2023, **145**, 15078–15083.